Supporting Information for "The interplay between seismic and aseismic slip along the Chaman fault illuminated by InSAR"

M. Dalaison[1], R. Jolivet[1,2], E. M. van Rijsingen[1,3], S. Michel[1]

[1]École Normale Supérieure, PSL University, CNRS U.M.R. 8538, Laboratoire de Géologie, Paris, France

[2]Institut Universitaire de France, 1 rue Descartes, 75005 Paris, France

[3]Department of Earth Sciences, Utrecht University, Utrecht, the Netherlands

---

Corresponding author: M. Dalaison, Laboratoire de Géologie, École Normale Supérieure, 24 rue Lhomond, 75005 Paris, France. (dalaison@geologie.ens.fr)

November 10, 2021, 4:15pm

Contents of this file

1. Text S1 to S3

2. Tables S1 to S4

3. Figures S1 to S26

Text S1. On the earthquake step amplitude *a priori*

The *a priori* range of a_j, the amplitudes of the Heaviside functions H_j, for each pixel depends on the Euclidean distance, d_j, to the earthquake epicenter. For a given pixel (superscript p), a_j are initially set to zero with *a priori* variance given by a two-dimensional Gaussian function centered on the earthquake epicenter with a maximum amplitude, b_j^2, and a characteristic width, w_j, that is

$$(\sigma_{a_j}^p)^2 = b_j^2 e^{-\frac{1}{2}\left(\frac{d_j^p}{w_j}\right)^2}.$$ (1)

Consequently the *a priori* standard deviation, $\sigma_{a_j}^p$, is also a two-dimensional Gaussian with a characteristic width equal to $\sqrt{2}w_j$ and a maximum amplitude of b_j (Figure S4). For all earthquakes, we choose to set the maximum standard deviation, b_j, to 30 mm and the width, w_j, to 9 km. This means that, for instance, $\sigma_{a_j}^p$ is 15 mm about 25 km away from the predicted earthquake location. Below a threshold of $\sigma_{a_j}^p = 1$, we set $\sigma_{a_j}^p$ to zero to avoid having small but non-zero covariance extending faraway from the earthquake and, thus, simplify the problem mathematically. With $w_j = 9$ km this threshold is reached at a distance of about 40 km from the earthquake location.

In addition to potential over-fitting of the data, another reason to limit the spatial extent of the modeled earthquake step is the impact of this additional parameter on velocity estimates. Indeed, there is an inter-dependency which arises mathematically between the earthquake step amplitude and velocity, which results in larger uncertainties (see map of velocity uncertainties in Figure S15).

Text S2. On the parametrization of the dislocation screw inversion

We model interseismic slip at depth on the Chaman fault (CF) using a dislocation screw model, an equation relating ground velocity as a function of the perpendicular distance to the fault to the amount of slip S below a locking depth D_S, and the amount of creep C above the creep extent D_C (Section 3.4) [Savage & Burford, 1973]. We adjust this model to 3556 profiles across the CF independently, allowing for an offset in the fault location X_f, a constant shift of velocities A and a ramp B. We invert for those 5 parameters using a Markov-Chain-Monte-Carlo algorithm implemented in the python package PyMC3 [Salvatier et al., 2016]. The description of the prior distribution of all parameters is in Table S2.

Our parametrization does not allow locking depths larger than 9 km because of the difficulty to distinguish the corresponding surface strain rates from a linear ramp on 30 km-long profiles. Longer profiles in the fault-related deformation would be affected by non-tectonic signal arising from the proximity of the Rigestan desert west of the CF. We consider velocity estimates and their associated uncertainties. Moreover, we add a prediction error of 2 mm/yr to all velocities, to account for the fact that the design of the model is source of additional uncertainties [Duputel et al., 2014]. The posterior probability density function, product of the prior probability density functions, and of a Gaussian likelihood function, is sampled with a Metropolis-Hastings algorithm through 4 independent chains of 10000 samples each; the 5000 first samples are burned.

Text S3. On the uncertainty propagation from interferograms to surface fault slip

Our time series analysis method (KFTS) estimate covariances for all parameters including interferometric phases at each time step and velocities [Dalaison & Jolivet, 2020]. Resulting standard deviations take into account predefined errors from phase misclosure and mismodeling (including temporally decorrelated noise like tropospheric delays), uncertainty coming from the structure of the interferometric network on a given pixel and trade-offs between describing parameters. Interferometric phase estimates are very precisely known. However, the interpretation of this phase in terms of deformation is associated with significant, hardly quantifiable uncertainty that is thought to be of the order of magnitude of the mismodeling error ± 10 mm [Dalaison & Jolivet, 2020].

Parameters of the time dependent model, like velocity, have non-negligible uncertainties (e.g. Figure S15). To get surface slip rates, we draw profiles in the velocity map (a_1 in Equation 1 or v_H in Equation 2) and in the map of the associated standard deviation, so that each measure of velocity, $v(x_i)$, at distance x_i from the fault along the profile has associated uncertainty, $\sigma_v(x_i)$ (Section 3.4). We compute the weighted mean velocity, $\bar{v}$, within 500 m and 1.5 km on each side of the fault. For instance, the formula for N points satisfying 0.5 km $< x_i <$ 1.5 km is

$$\bar{v}^{\text{right}} = \sum_{i=1}^{N} \frac{v(x_i)}{\sigma_v(x_i)^2} \times \left(\sum_{i=1}^{N} \left(\sigma_v(x_i)^2 \right)^{-1} \right)^{-1}. \tag{2}$$

There are two ways to compute the error associated to the mean value: we can either propagate the known uncertainties $\sigma_v(x_i)$ (i in $[1, N]$) assuming uncorrelated measurements or

compute the standard deviation of the N averaged $v(x_i)$. While the first definition takes into account observational error, the second quantifies the amount of spatial scattering in velocity estimates. For each $\bar{v}$, we choose the definition leading to the largest error $\sigma_{\bar{v}}$. Numerically, it writes as

$$\sigma_{\bar{v}} = MAX \left[\sqrt{\left(\sum_{i=1}^{N} (\sigma_v(x_i)^2)^{-1} \right)^{-1}}, \sqrt{\frac{\sum_{i=1}^{N}(v(x_i) - \bar{v})^2}{N}} \right]. \tag{3}$$

Consequently, the surface slip rate standard deviation, σ_{dv}, is

$$\sigma_{dv} = \sqrt{(\sigma_{\bar{v}}^{left})^2 + (\sigma_{\bar{v}}^{right})^2}. \tag{4}$$

As a result of this two-folded definition, we obtain a conservative estimate of across fault slip uncertainty for da_1 and dv_H (Figure 5c,d), meaning that the uncertainty is likely smaller than what we estimate. This outlines the robustness of our slip measures.

Date (UTC)	Longitude	Latitude	Depth (km)	M_w	Numb. of events	Total M_w
2015/08/03 13h16	66.020	27.370	12	5.4	3	5.57
2016/03/21 14h48	66.140	27.747	14.9	5.7	10	5.73
2016/05/13 6h59	66.472	30.633	12.6	5.6	3	5.74
2016/07/10 21h33	66.580	30.780	15	5.1	1	5.1
2018/06/27 16h53	66.334	30.495	12	4.1*	2	4.52

Table S1.   Detailed information about earthquakes taken into account in our InSAR time series analysis from the Global Centroid-Moment-Tensor (GCMT) project and the International Seismological Center (ISC) bulletin (see Section 2.2) [Dziewonski et al., 1981, Ekström et al., 2012, *ISC On-line Bulletin*, 2020, Bondár & Storchak, 2011]. Each event can correspond to a group of closeby earthquakes, which may not be distinguishable at the scale of InSAR time series. Properties of the main (i.e. largest M_w) earthquake are in the first five columns. The number of events within 20 days and 40 km of the main event (Figure S1) is in the sixth column. The corresponding total moment converted to M_w is in the last column with some uncertainty linked to the conversion from m_b to M_w [Scordilis, 2006]. (*) The last magnitude is a body-wave magnitude (m_b).

Name	Bounds	Mean	Std	Unit
Constant A	-10, 10	-	-	mm/yr
Ramp, B	-0.5, 0.5	0	0.05	(mm/yr)/km
Creep, C	0, 30	-	-	mm/yr
Creep extent, D_C	0, 8	1	3	km
Slip, S	0, 30	-	-	mm/yr
Locking depth, D_S	0.01, 9	2	5	km
Fault location, X_f	-1.2, 1.2	0	0.25	km

Table S2.   Descriptive parameters for prior distributions used in our dislocation model inversion for slip along the Chaman fault during the interseismic period. The three parameters with no mean or standard deviation (std) specified have uniform distributions.

November 10, 2021, 4:15pm

Source	Number of earthquakes	Minimum M_w	Maximum M_w	1900-2019 M_o (Nm)	1990-2019 M_o (Nm)
GCMT	8	4.9	5.9	1.69×10^{18}*	7.29×10^{17}
USGS	85	3.6	6.7	2.38×10^{19}	8.89×10^{17}
ISC	139	3.8	6.5	1.79×10^{19}	1.57×10^{18}

Table S3.   Statistics of the seismicity within 30 km of the Chaman fault. *GCMT catalog starts in 1976.

Date (UTC)	Pre-seismic (mm/yr)	Coseismic (mm)	Early postseismic (mm)	long-term postseismic (mm)	postseismic period (days)	postseismic to coseismic
2016/05/13	1.2	11.7	11.9	4.6	521	1.3
2016/07/10	1.1	13.5	4.0	3.6	595	0.4
2018/06/27	2.4	8.8	6.1	2.8	346	0.8

Table S4.   Peak-to-peak surface slip in profiles of Figure 8 across earthquake-related displacement as considered in Section 5.2. Those values are indicative and used to compute postseismic to coseismic slip ratios only, defined as : [early postseismic + long-term postseismic − preseismic slip × postseismic period/365] / coseismic .
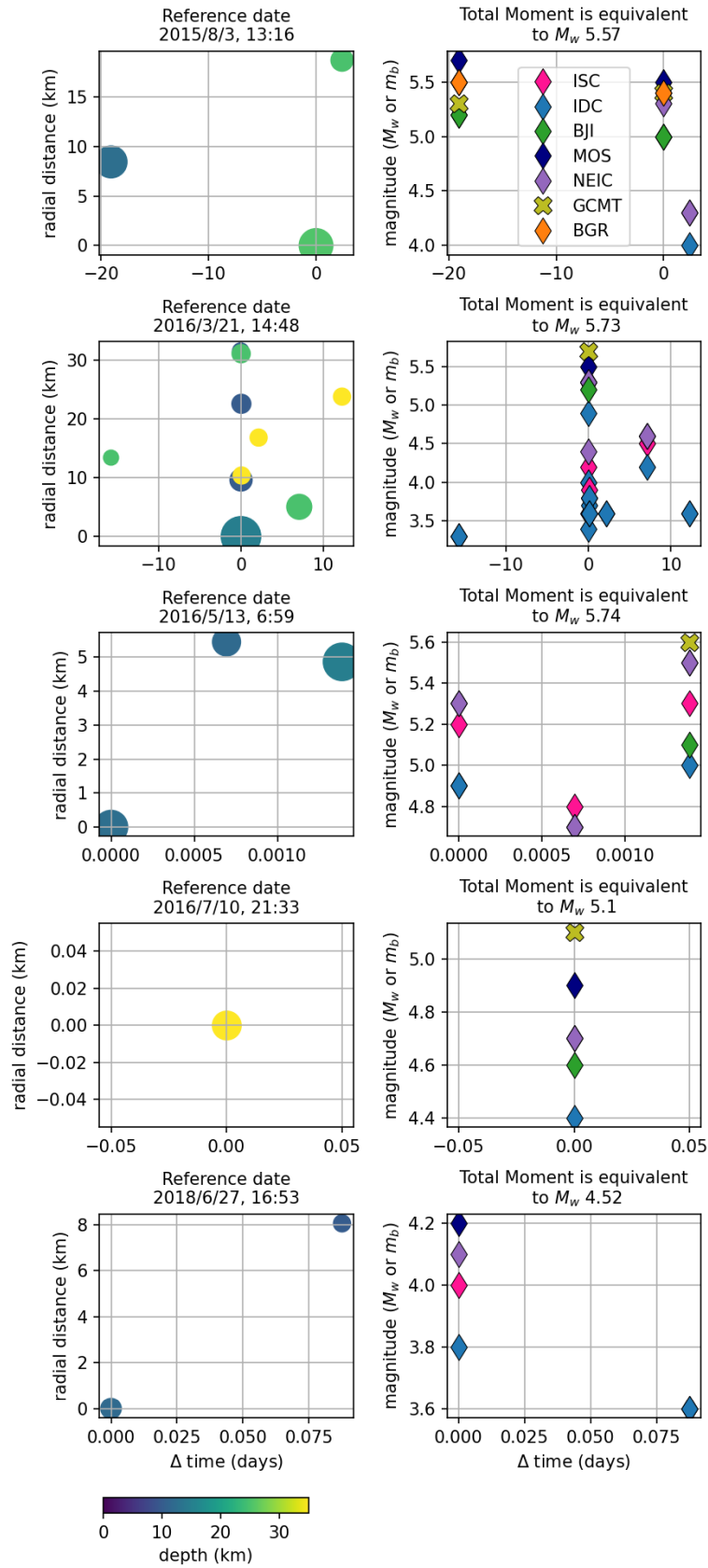
Figure S1.

November 10, 2021, 4:15pm

Figure S1.   (Previous page) Timing and magnitude estimates from the International Seismological Center (ISC) Bulletin [consulted in August 2019] of earthquakes in spatio-temporal proximity to the studied events (Table S1). The left column displays the spatio-temporal relationship of events within 20 days and 40 km radius around each of the five studied earthquakes. The size of the marker is scaled with its magnitude and its color reflects the estimated depth. The right column shows the range of magnitude estimates from different sources (seismological institutes). The color of the marker depends on the source (legend in top right plot): ISC, International Data Centre (IDC), China Earthquake Networks Center (BJI), Geophysical Survey of Russian Academy of Sciences (MOS), National Earthquake Information Center (NEIC), Global CMT Project (GCMT), Bundesanstalt für Geowissenschaften und Rohstoffe (BGR). Two types of magnitude estimates are shown: crosses are M_w (only from GCMT), while diamonds are m_b. The total moment is computed using the M_w when available or the mean m_b value converted to M_w using Scordilis [2006]'s relationship.
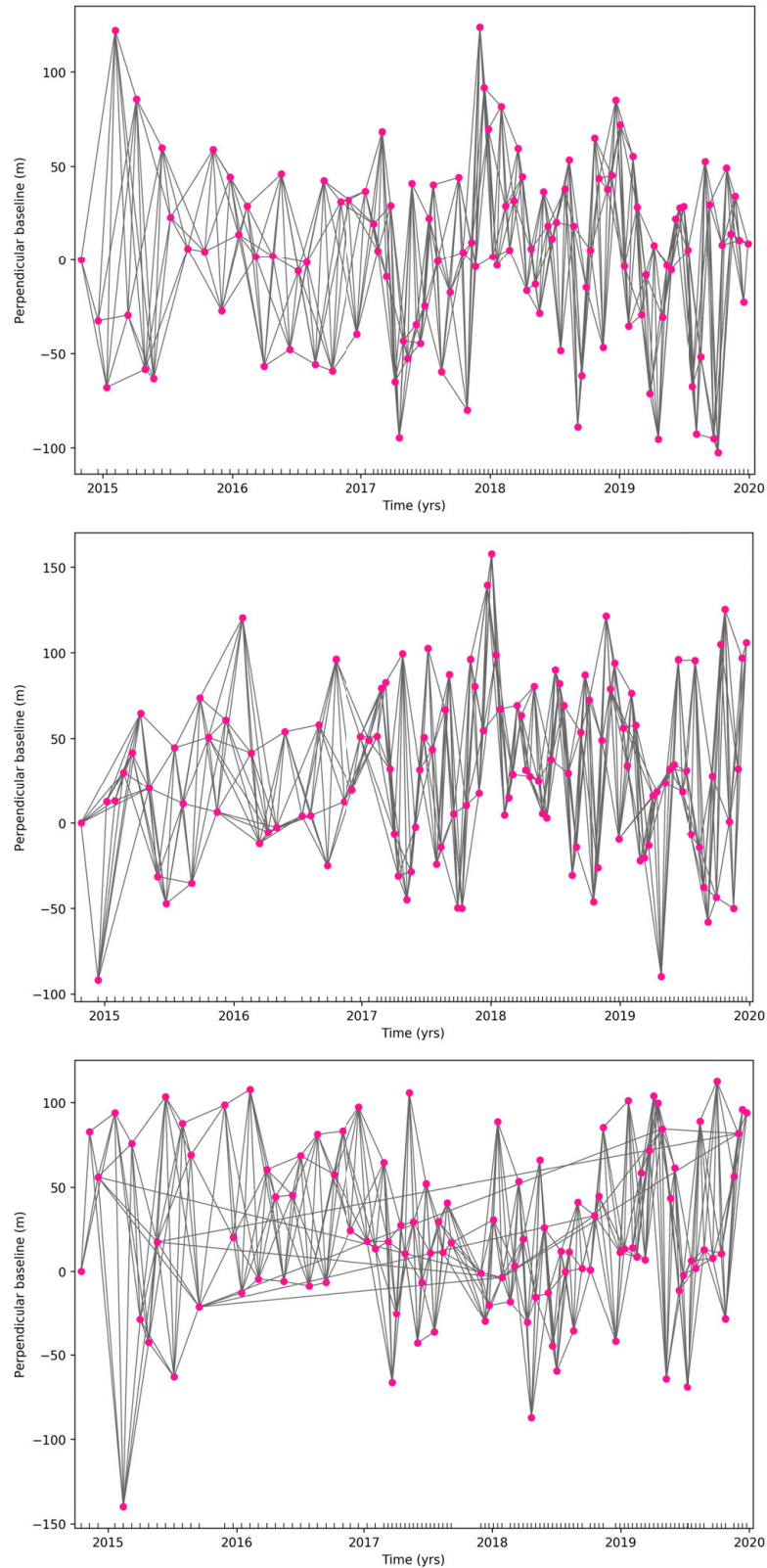
Figure S2.   Perpendicular baseline versus date of acquisitions for the three Sentinel 1A-B

ascending tracks 42 (top) and 144 (middle) and descending track 151 (bottom). Each dot is a

SAR acquisition and connecting lines are interferograms. Perpendicular baseline refers to orbital

November 10, 2021, 4:15pm

configuration during acquisitions.
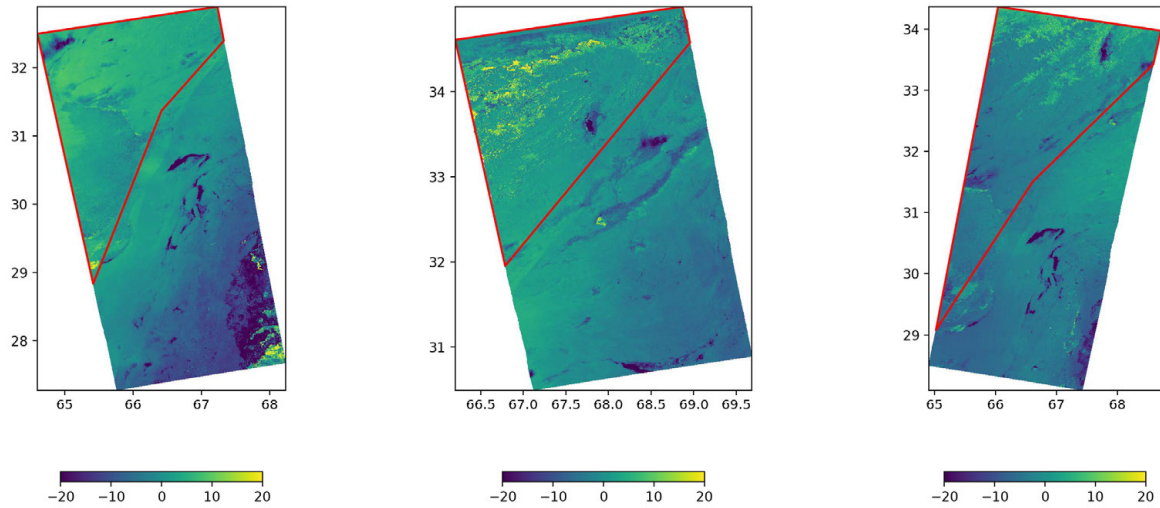
Figure S3.   Red line delimits the reference zone used for deramping interferograms on tracks 42 (Left), 144 (Middle) and 151 (Right). The average velocity field is in the background for easier spatial reference (in mm/yr).
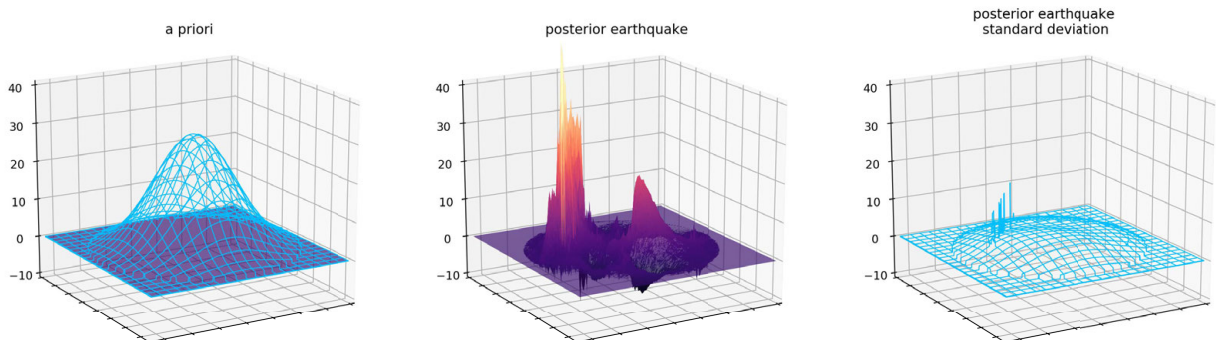
Figure S4.   Representation of the *a priori* for the parameter corresponding to earthquake amplitudes (left) and example of the final estimate for the 13 May 2016 earthquake (center and right). Horizontal axes are spatial directions, while the vertical axis shows the earthquake amplitude and uncertainties in millimeters. Colored surfaces are earthquakes amplitudes and blue meshes are the associated standard deviations. The center plot contains the same data as Figure 2e in a 3-D projection.
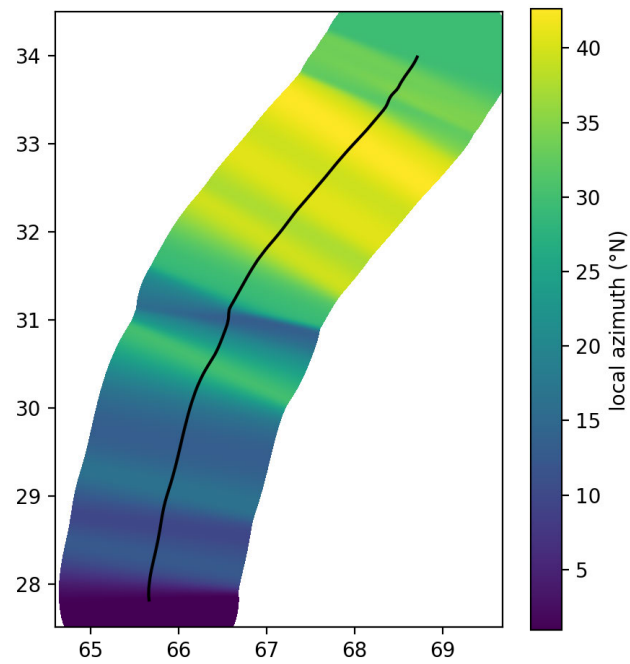
Figure S5. Fault azimuth map used as projection angle in Figure 3.
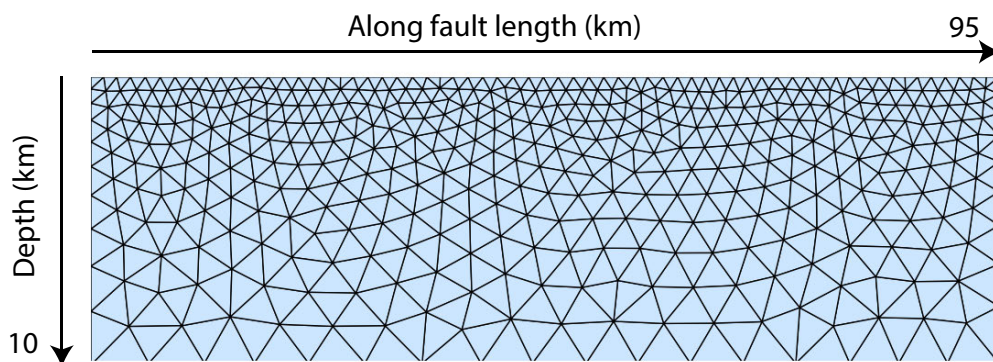
Figure S6. Mesh of the fault for source modeling of the three Chaman fault earthquakes.

November 10, 2021, 4:15pm
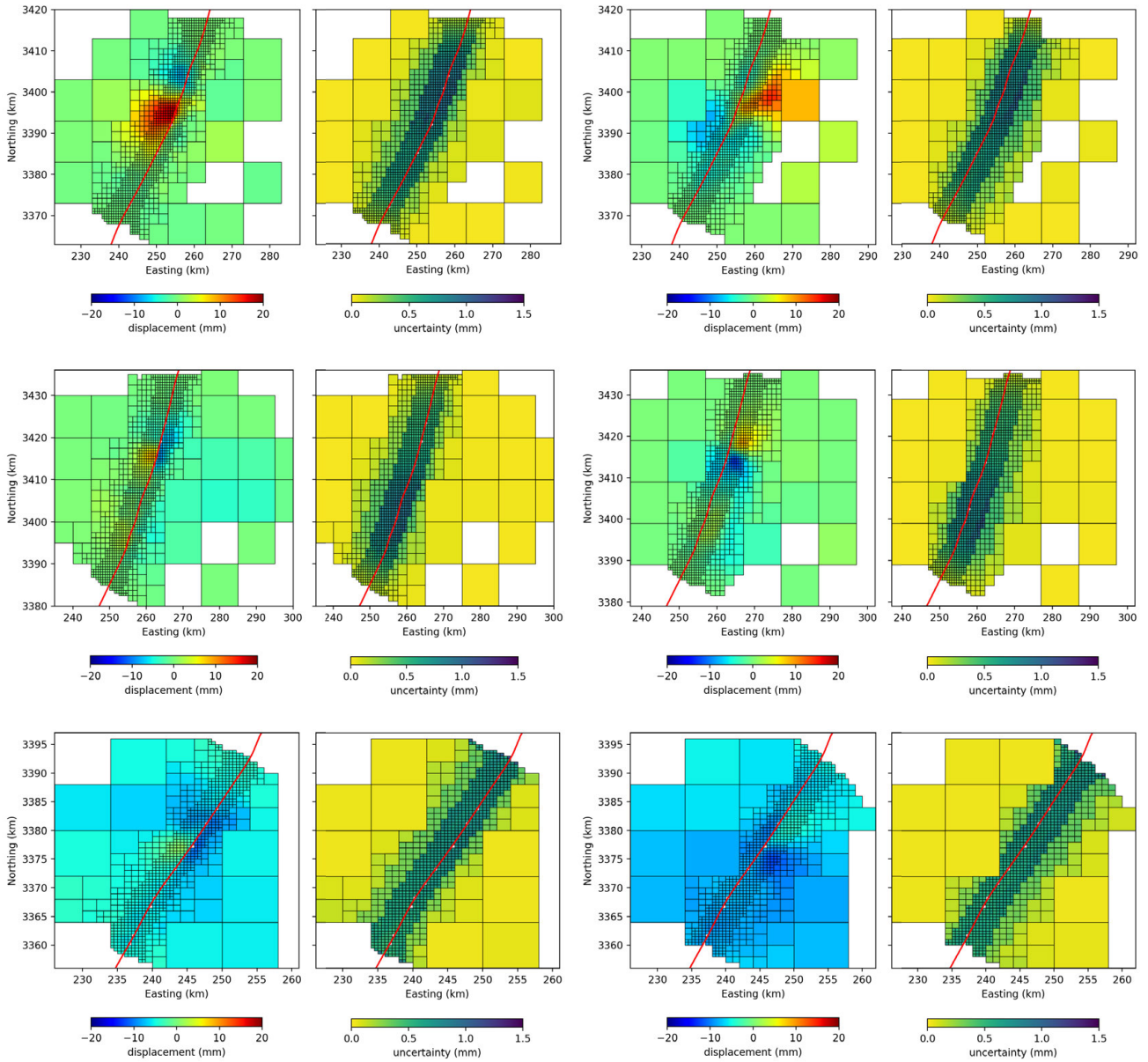
Figure S7. Downsampled coseismic displacement and associated uncertainties using a quadtree scheme. Observations along ascending (left column) and descending (right column) tracks are shown for each earthquake: 13 May 2016, 10 July 2016, 27 June 2018 (from top to bottom).
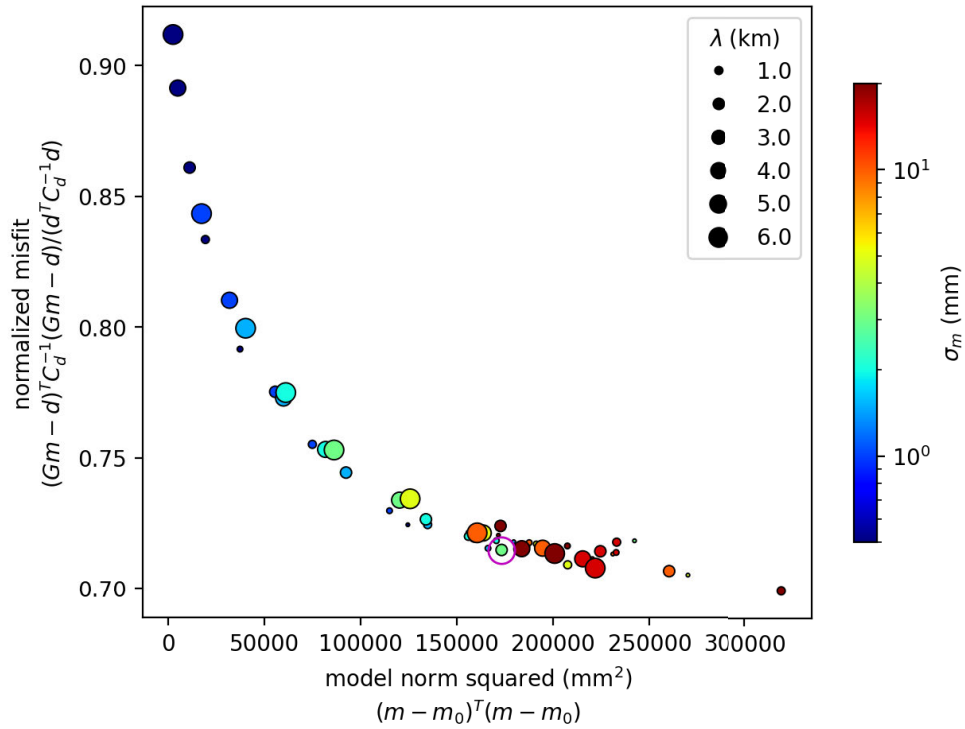
Figure S8.   L-curve to optimize parameters of the *a priori* model covariance: the characteristic length (λ) and model standard deviation (σ_m) [Radiguet et al., 2011]. In violet is surrounded the chosen parameter λ=2 km σ_m= 3 mm. This is for the first earthquake only, taken as a representative example for the three events.
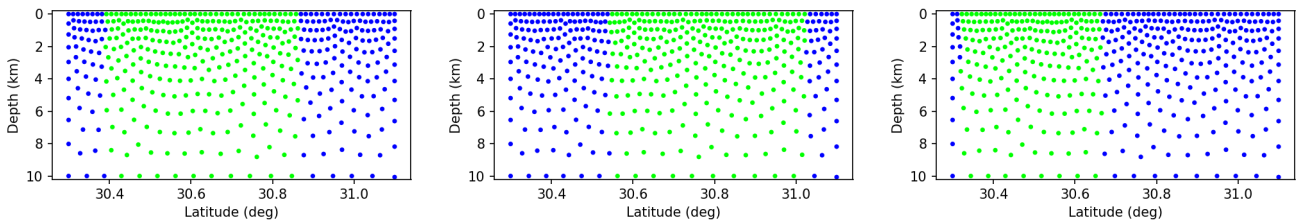

Figure S9.   Variations in σ_m and thus of the diagonal of the model covariance matrix C_m as a function of the localization of the fault patch center for our three inverted earthquakes : May 2016 (left), July 2016 (center), June 2018 (right). Light green nodes are for σ_m=2 mm and blue nodes for σ_m= 1 mm (outside of data footprint).

November 10, 2021, 4:15pm
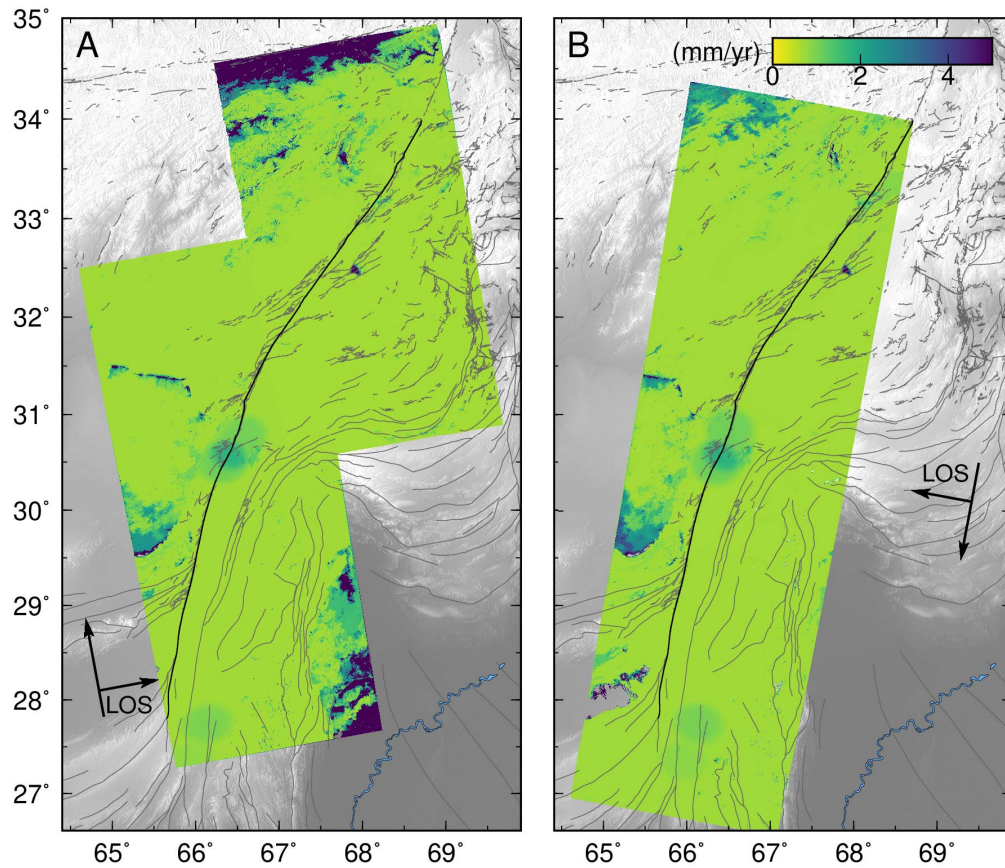
Figure S10.   Maps of standard deviations of velocity fields shown in Figure 2 for ascending tracks (A) and the descending track (B) in the Line Of Sight (LOS) direction. Our velocity estimates are mean rates of phase change and not rates of deformation, because this is what InSAR measurements contains (Section 3.1). Therefore, uncertainties do not reflect whether or not the observed phase change arises from non-tectonic sources of phase change (e.g. atmosphere).

November 10, 2021, 4:15pm
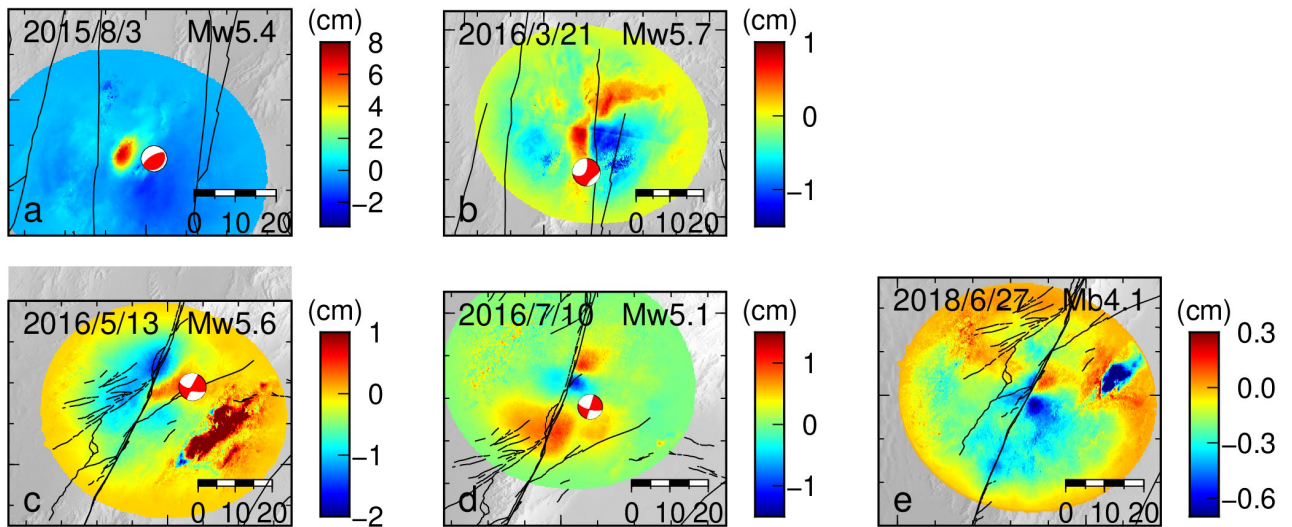
Figure S11.   Estimated coseismic displacement according to our parametrized model of deformation for the descending track (T151). The same observations for the ascending track (T42) is in Figure 2c-g with the location of frames in Figure 2a.
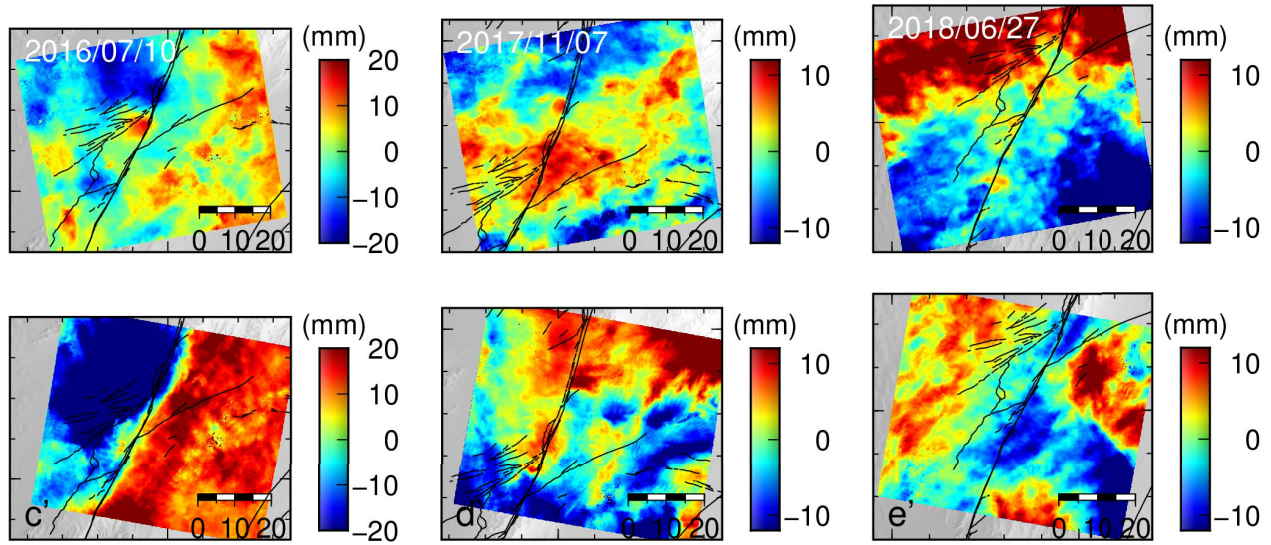
Figure S12. View of the coseismic earthquake displacement measured as the difference between acquisitions right before and after each event for the three events close to the city of Chaman. Because each pattern is the phase difference between acquisitions before and after each event, it includes turbulent atmospheric delays. Those undesired atmospheric delays are temporally decorrelated and, thus, tend to average out when looking at the time series as a whole, justifying our preference for the parametric model solution to characterize earthquake induced deformation, although it does include some post-seismic signal. Ascending (top row) and descending (bottom row) data are displayed.
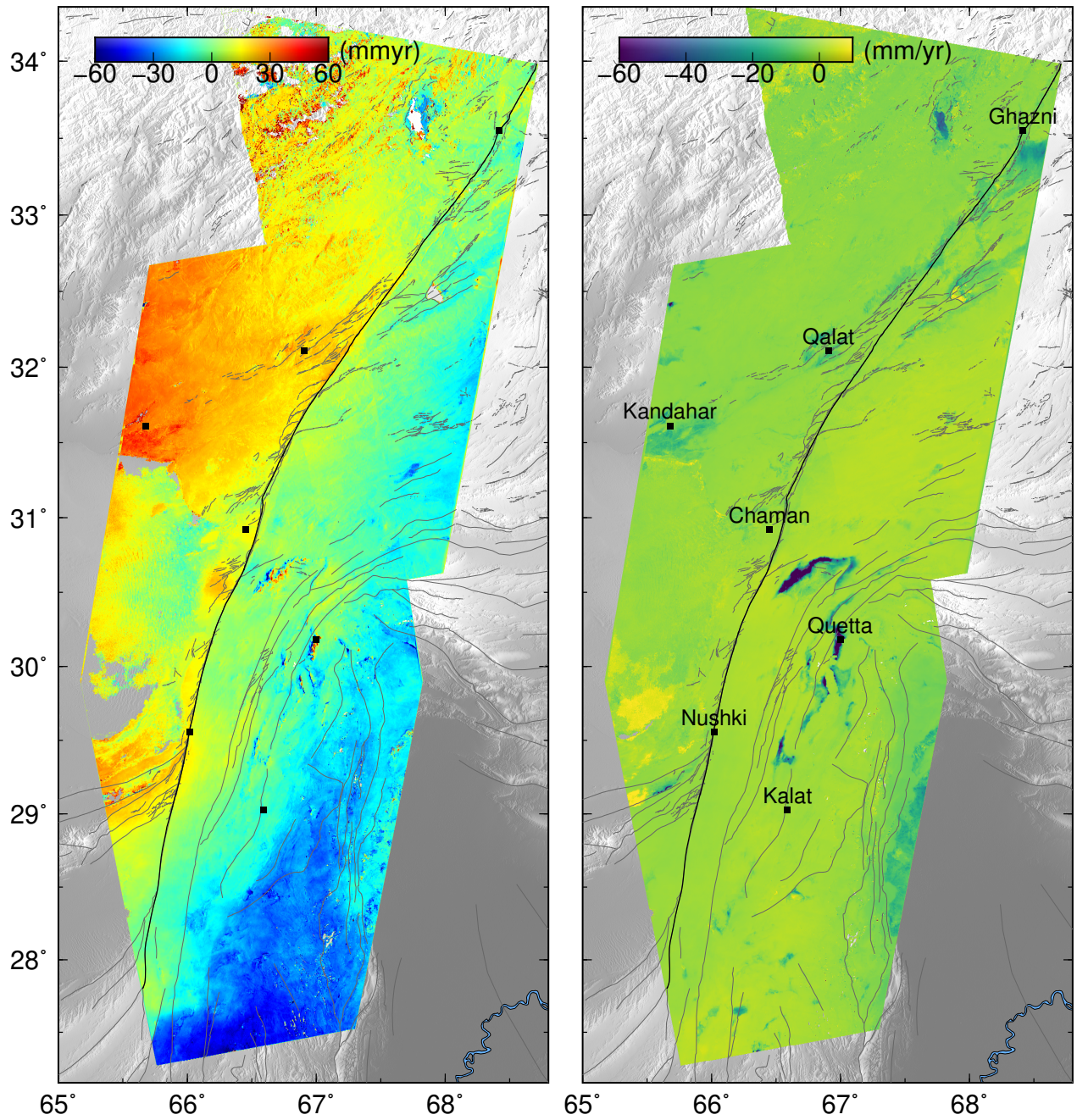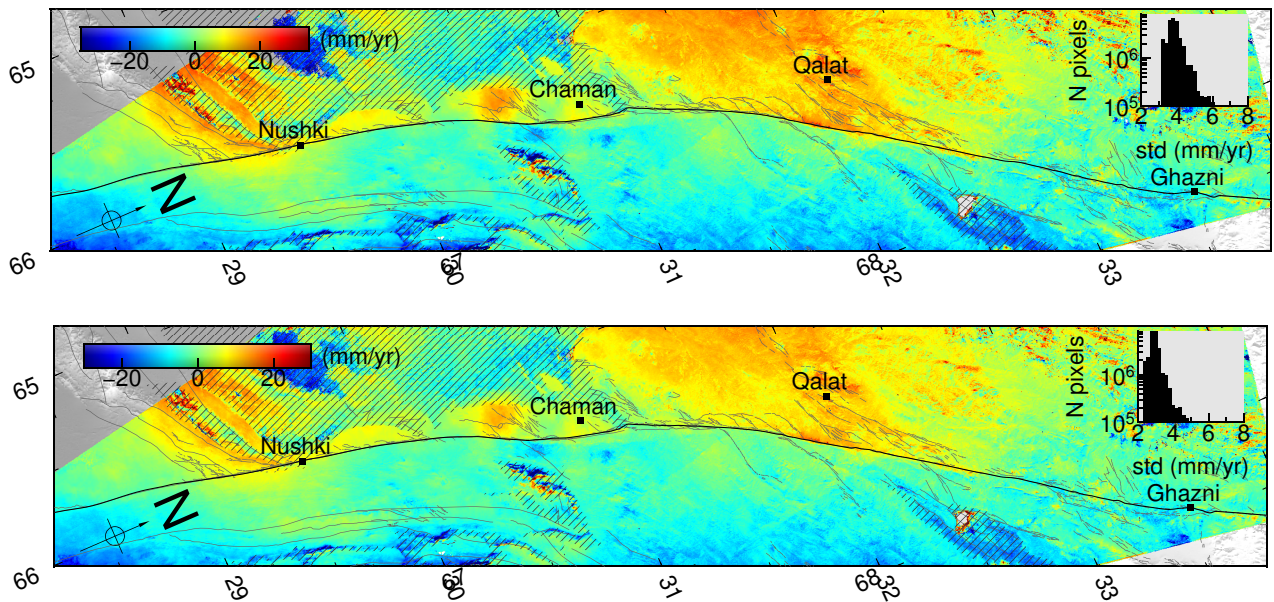
Figure S13. Velocity field when projected in the 15°N direction (close to IN-EU plate motion, left) and associated vertical velocities (right). Data with standard deviation >6 mm/yr is masked. Maximum subsidence rate exceeds the colorbar limit (see Figure S14).

November 10, 2021, 4:15pm
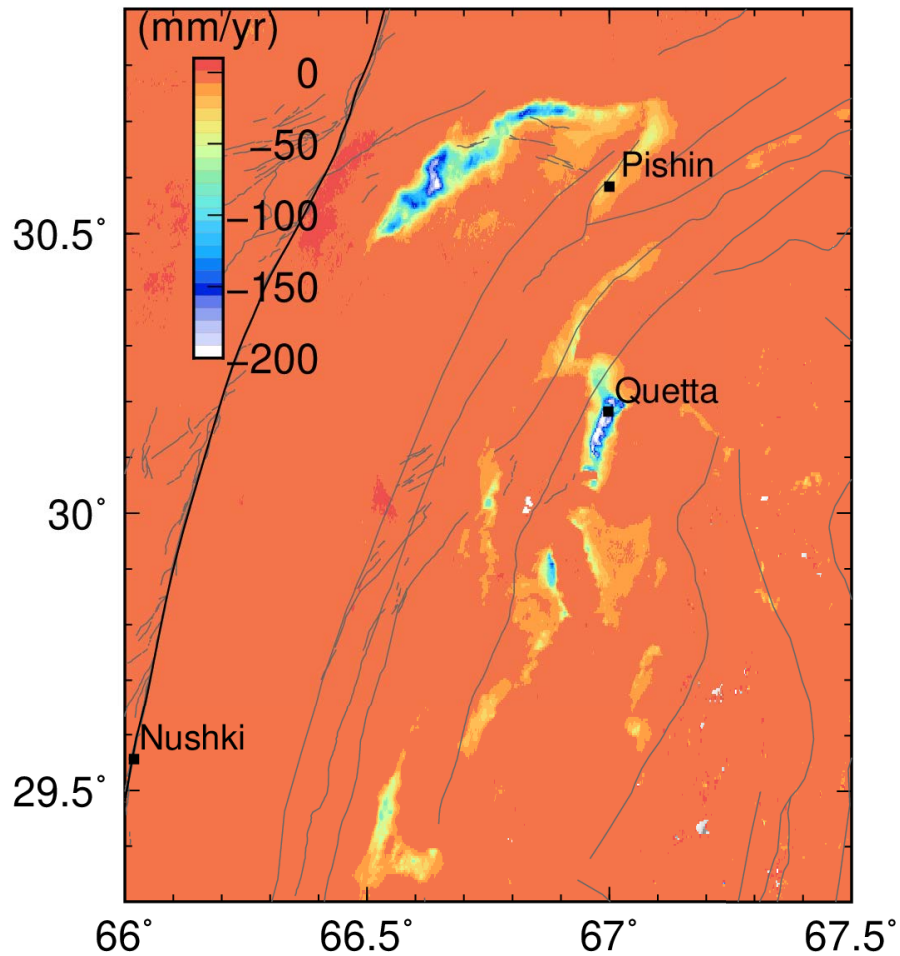
Figure S14.   Zoom on the subsidence rate according to our vertical decomposition of the signal. Same data as Figure S13 (right subplot) but with a different color scale, suited for high subsidence rates within regions of dense human occupation (e.g. Pishin basin, Quetta). Subsidence originates from the massive groundwater decline recorded in Quetta (up to 5-15 m/yr locally), a resource under great stress from recent climatic and demographic trends: more drought and a dramatic growth of Quetta valley population and cultivated area in the past 30 years [Kakar et al., 2016].
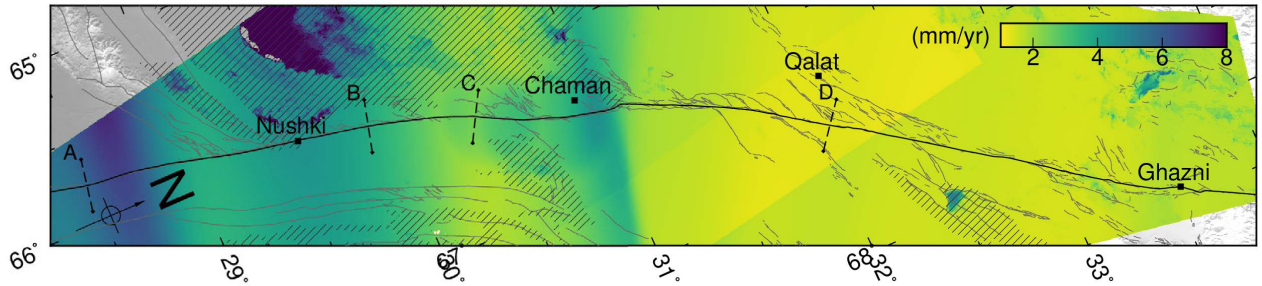
Figure S15. Map of the standard deviations of the velocity field projected in fault parallel direction shown in Figure 3.


Figure S16. Same as the map in Figure 3 for different angles of projection. Velocity field when projected in the 15° North (top) and 20° North (bottom) directions (close to IN-EU plate motion) with associated histograms of standard deviations (std).

November 10, 2021, 4:15pm
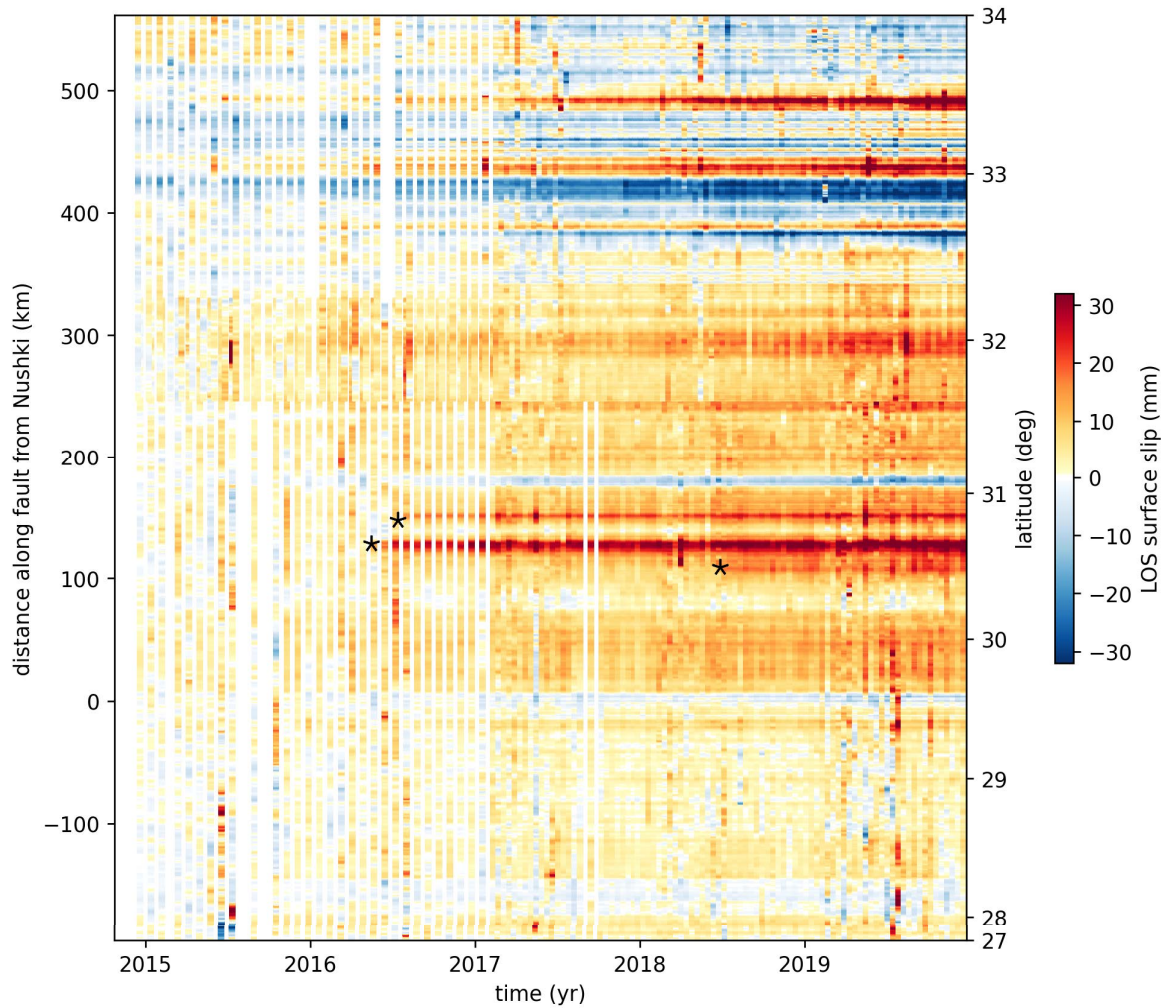
Figure S17.   Same as Figure 4, but with a measurement of surface slip based on points at a distance between 1 to 5 km from the fault trace instead of 500 m to 1.5 km.

November 10, 2021, 4:15pm
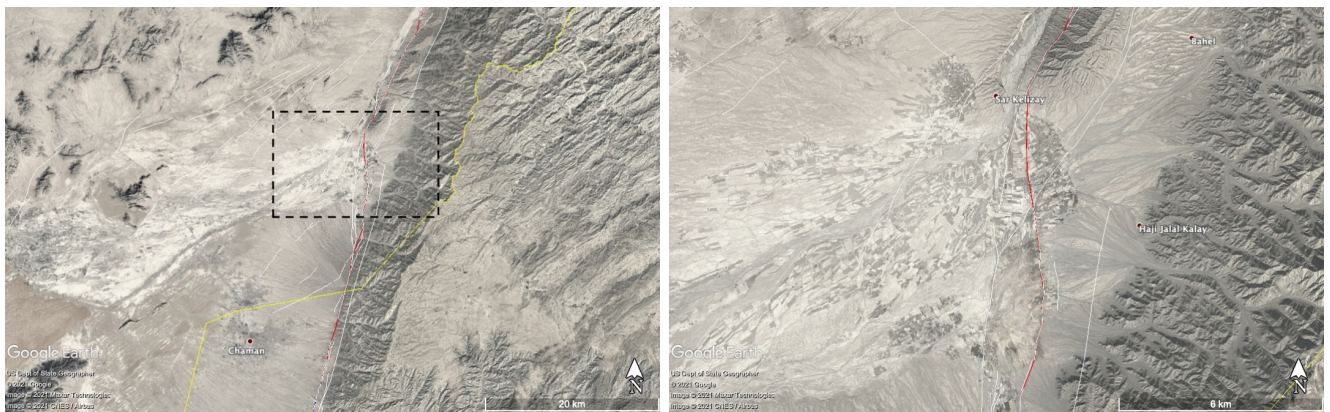
Figure S18.   Optical images of the ground near the Chaman fault main releasing bend from Google Earth. White lines are fault traces from Ruleman et al. [2007], the red line is our continuous fault trace, the yellow line is the frontier between Pakistan and Afghanistan. Agricultural fields and human settlement cluster around the Dori River producing a negative anomaly in velocities west of the fault.
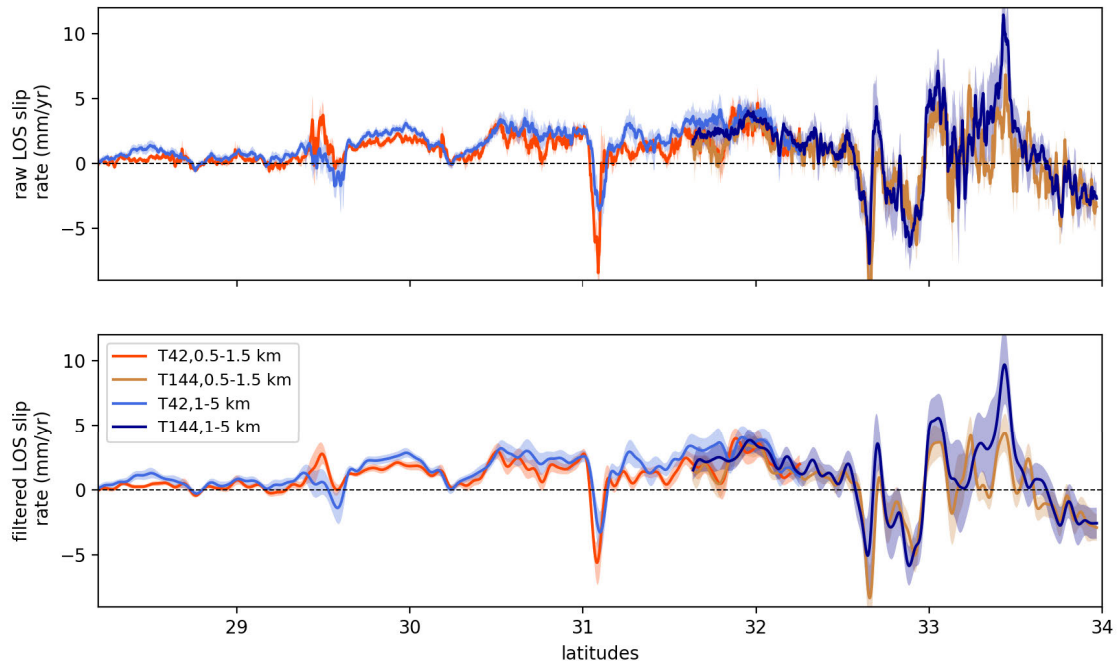
Figure S19.   More details on the line of sight (LOS) surface slip rate measures displayed in Figure 5b. Orange and blue lines are the raw (top) and filtered (bottom) surface slip measured along strike with two different spatial footprints of 0.5-1.5 km and 1-5 km, respectively. Measures from both ascending tracks are shown (track 42 and 144). The spatially low-pass filtered surface slip rate between 0.5 and 1.5 km off the fault trace are the same as in Figure 5b.
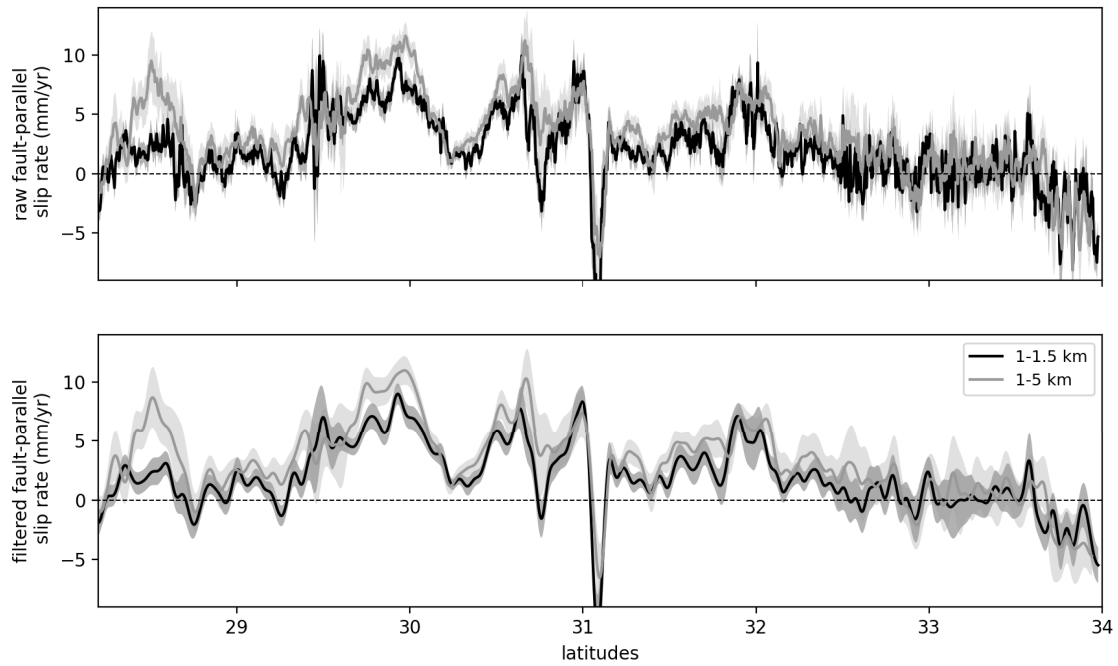
Figure S20.   More details on the slip rates projected in the fault-parallel direction displayed in Figure 5c. Black and gray lines are the raw (top) and filtered (bottom) strike-slip motion measured along strike with two different spatial footprint of 0.5-1.5 km and 1-5 km, respectively. The spatially low-pass filtered strike-slip component (black curves in bottom plot) is the same as in Figure 5c (against latitude instead of distance).
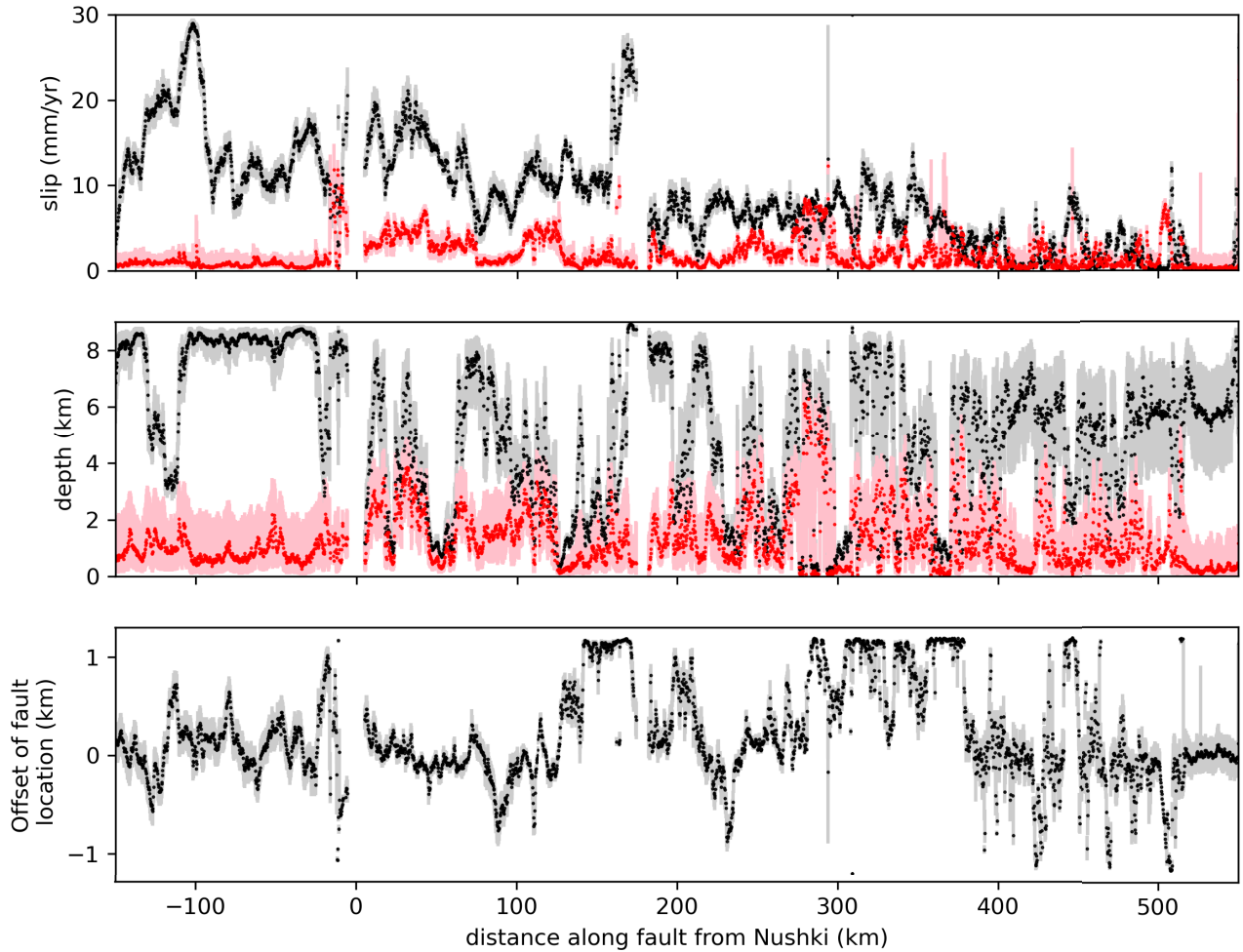
Figure S21.   Estimated median and interquartile range for the optimized parameters of our dislocation model on a vertical left-lateral fault (Equation 3, Section 3.4) along the Chaman fault trace. Parameters describing fault slip are: slip rate at depth S (top in black), creep rate C (top in red), locking depth D_S (middle in black), creep extent D_C (middle in red) and Chaman fault offset X_f (bottom). We prefer the median and interquartile range instead of the mean and standard deviation as the *posterior* probability density function is often asymmetrical, and thus not Gaussian, due to the bounded positive space explored (especially creep rates and depths). The model is adjusted to 15-km-long profiles of fault-parallel velocity every 200 m along the fault (like profiles in Figure 3).

November 10, 2021, 4:15pm
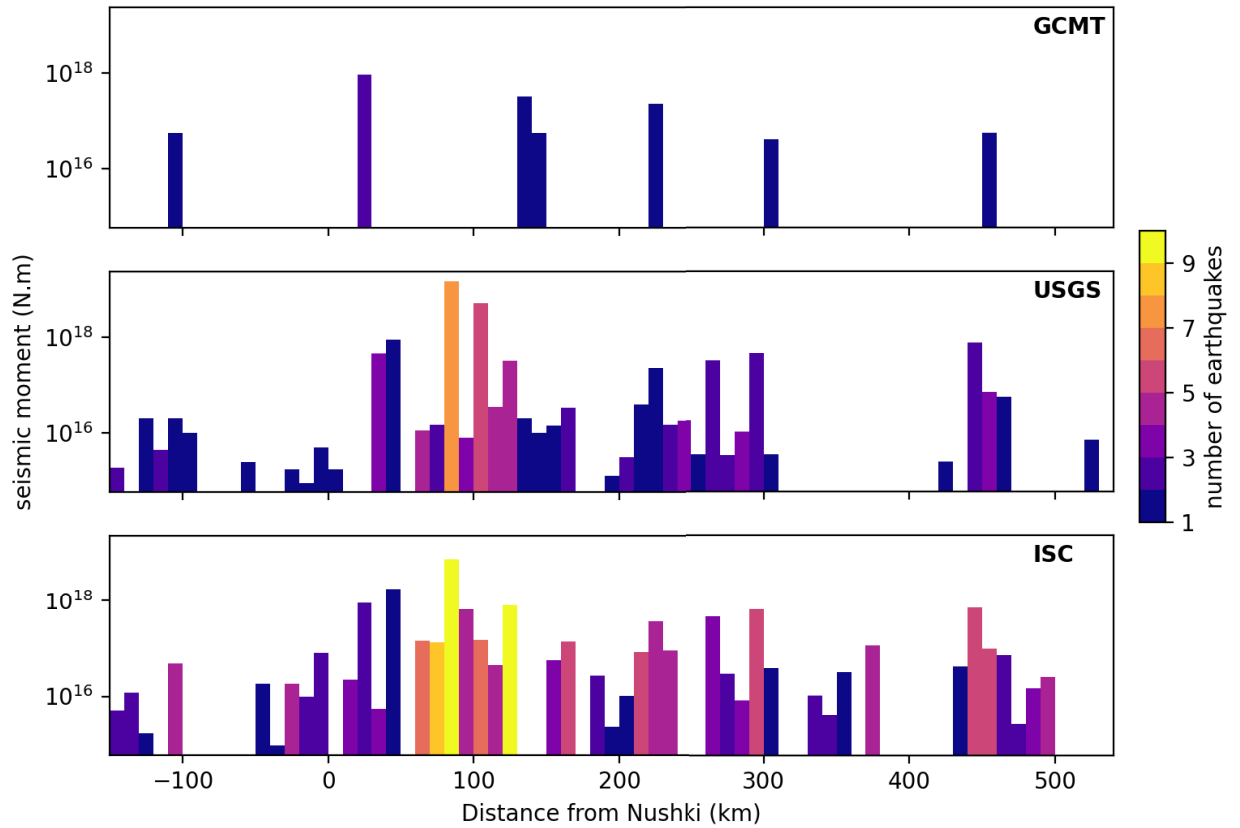
Figure S22. Distribution of seismic moment released along the Chaman fault (including events within 30 km) according to three sources : Harvard Global Centroid Moment Tensor (top), US Geological Survey (center), International Seismological Center (bottom; same as Figure 5e). The 10 km wide bars have heights equal to the sum of seismic moments release on the fault segment over 1990 to 2019 (plain and outlined bars) or over 1900 to 2019 (shaded bars). Colors reflect the number of events contributing to the total moment released in each bin.
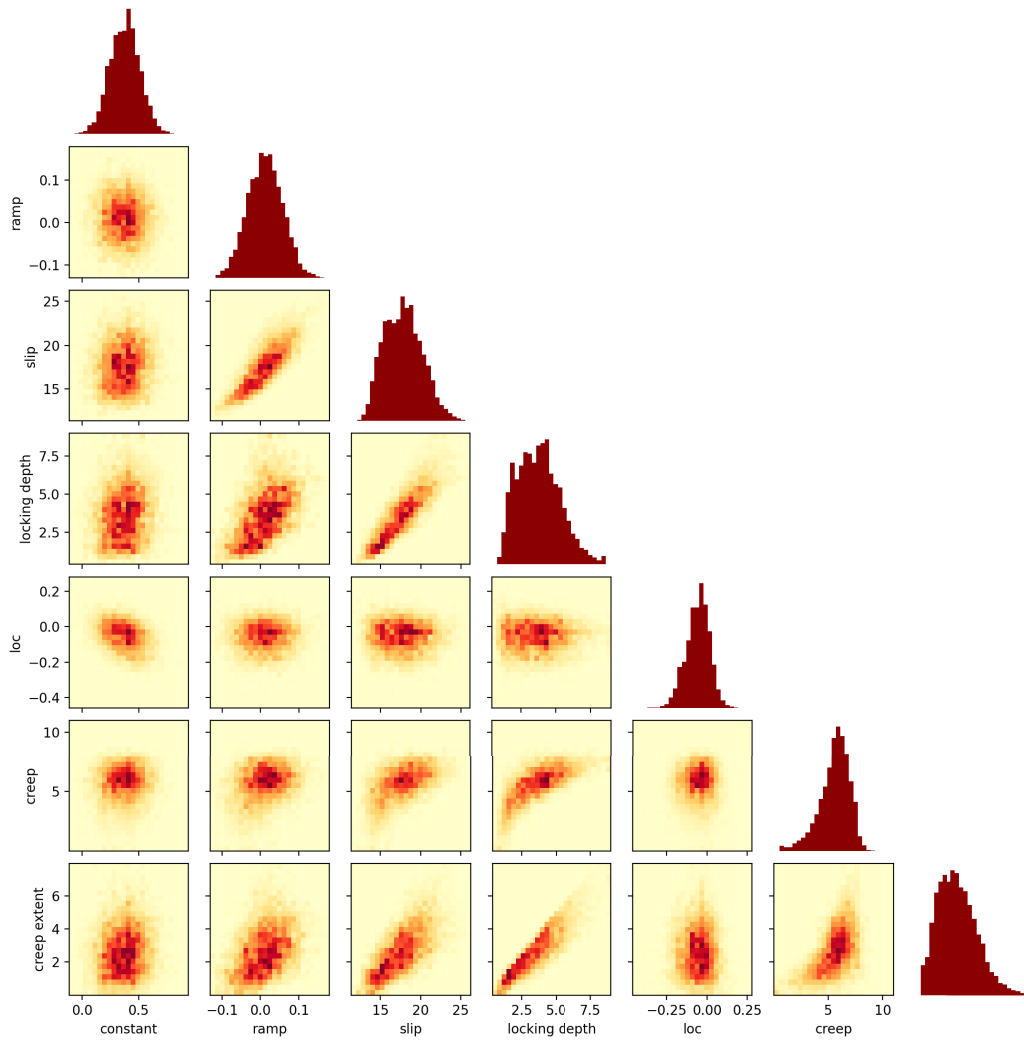
Figure S23.   Marginal posterior density distribution of model parameters (bar chart on the diagonal) and joint distributions (2D-histogram with higher sample density in dark red) for profile B in Figure 3 located 40 km north of Nushki. Parameters are described in Section 3.4 and listed in Table S2. They are a constant (A) in mm, a ramp (B) in mm/km, slip rate at depth (S) in mm/yr, locking depth (D_S) in km, fault location (X_f) in km, creep rate (C) in mm/yr, creep extent (D_C) in km. The elongated shape of the joint distribution S-D_S and S-B, exhibits a trade-off between those three parameters. The joint distributions involving C and D_C show a correlation of the creep estimate with D_S and S, showing the difficulty to distinguish shallow creep from slip at depth when D_S is close to D_C. This suggests a fault plane that slips from the surface to at least 9 km depth. The sharp bound of the D_C-D_S distribution along the $D_C = D_S$ line arises from the requirement of $D_C \leq D_S$.

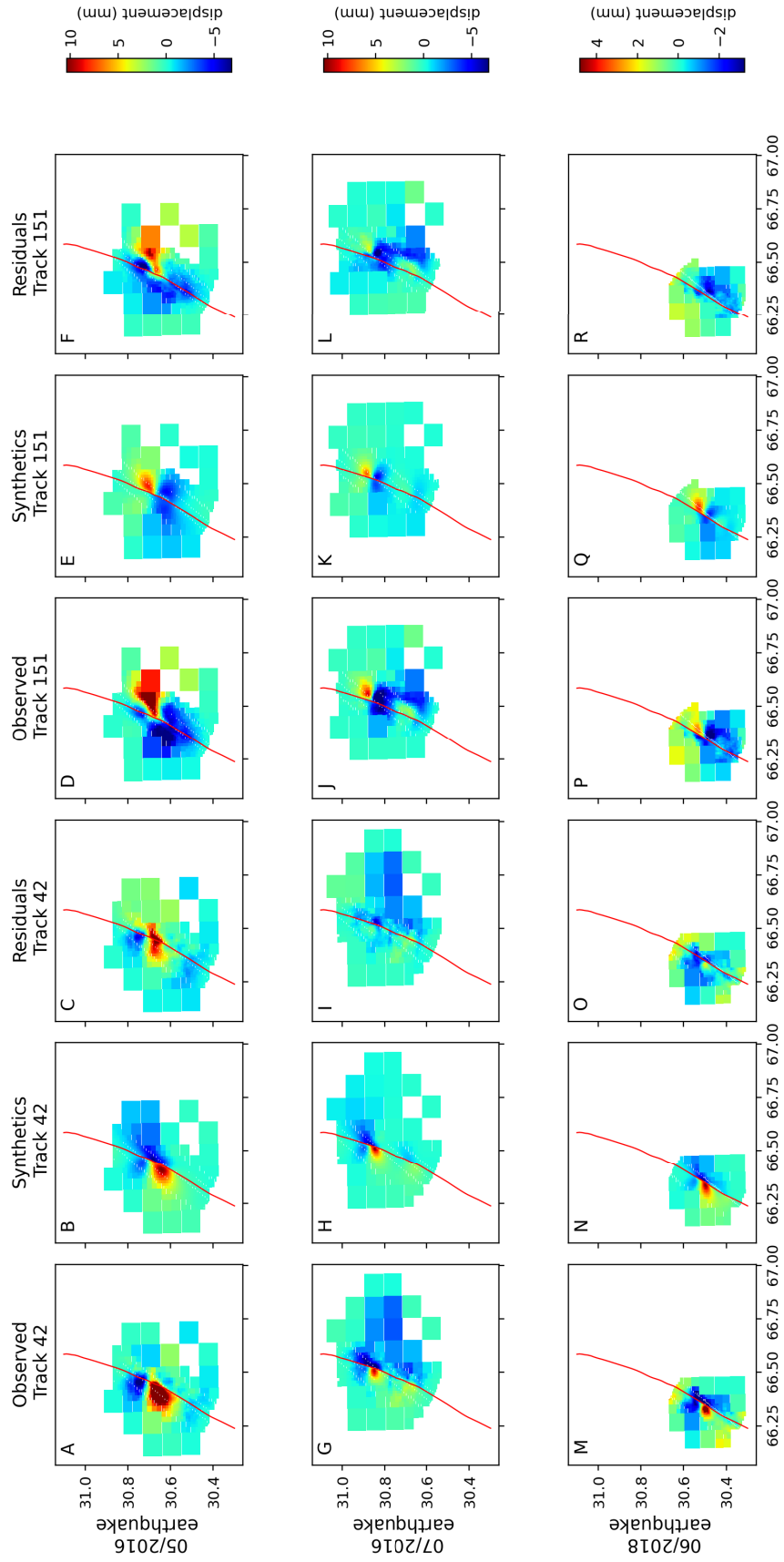November 10, 2021, 4:15pm

Figure S24.

November 10, 2021, 4:15pm

Figure S24.   (Previous page) Comparison of observed and modeled surface deformation due to three earthquakes on the Chaman fault. Each row is a different earthquake. The three columns on the left are in the ascending LOS (track 42), while the remaining columns are in descending LOS (track 151). Individual columns contain : observed deformation (A, G, M and D, J, P), synthetic deformation as predicted by modeled slip on the Chaman fault (Figure 7) (B, H, N and E, K, Q) and residual deformation in data once modeled slip is subtracted (C, I, J and F, L, R). Coarse patches far from the fault are the result of our downsampling. In red is the modeled fault trace. Colorbars apply to each row.
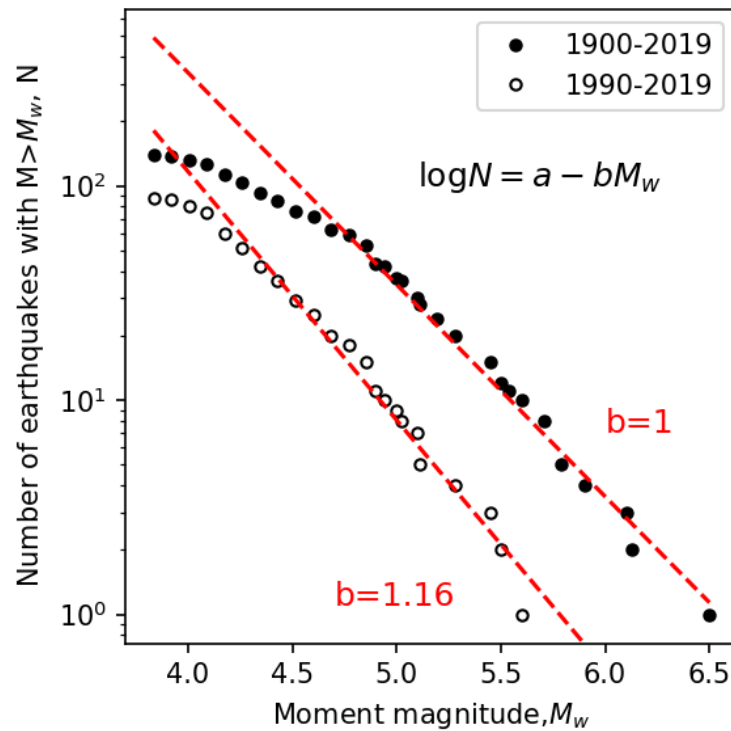
Figure S25.   Frequency magnitude plot for all earthquakes along the Chaman fault according to the International Seismological Center (ISC) catalog. The Gutenberg-Richter law is adjusted to two samples of the catalog covering 1900-2019 (filled circles), and 1990-2019 (outlined circles), 2019 included, and the b-value deduced (red text and dashed lines).

November 10, 2021, 4:15pm
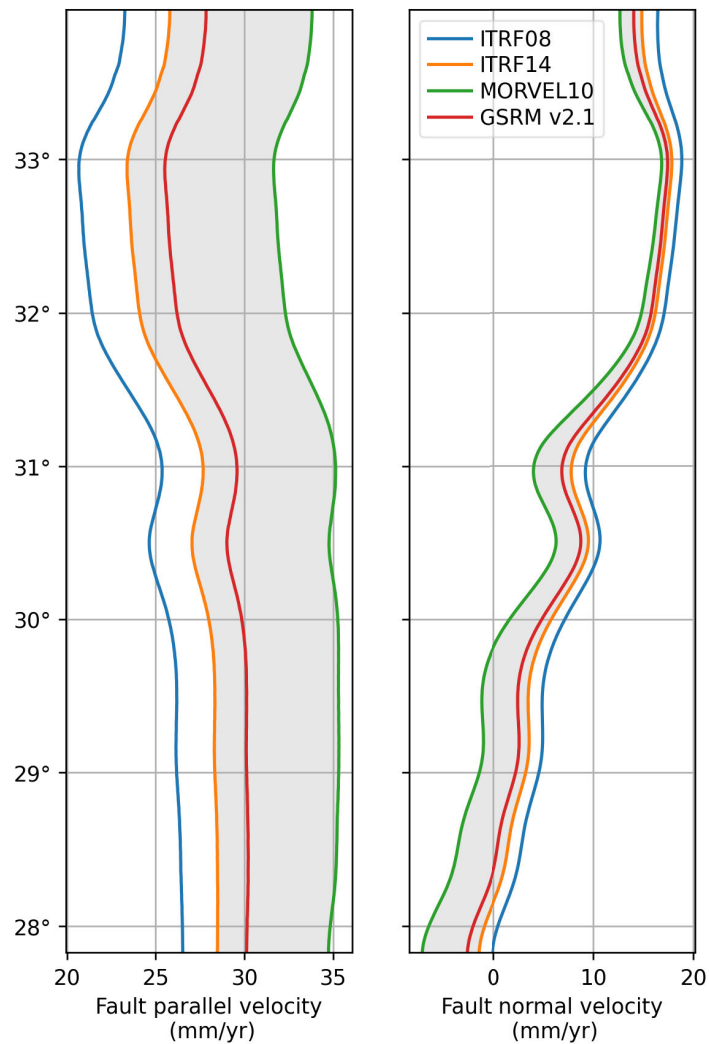
Figure S26. Global plate motion of India with respect to Eurasia as predicted by four published models projected along our fault-parallel (left plot) and fault-perpendicular (right plot) directions of the Chaman fault. ITRF08 is from Altamimi et al. [2012], ITRF14 from Altamimi et al. [2017], MORVEL10 from DeMets et al. [2010] and GSRM v2.1 from Kreemer et al. [2014]. Because ITRF14 is an update of ITRF08, we do not consider ITRF08 in our main text discussion. Thus, our likely relative plate motion is the region shaded in grey. ITRF08 is used as a reference in Szeliga et al. [2012]'s study of the Chaman fault (their Figure 13).

References

Altamimi, Z., Métivier, L., & Collilieux, X. (2012). ITRF2008 plate motion model. *Journal of geophysical research: solid earth*, *117*(B7).

Altamimi, Z., Métivier, L., Rebischung, P., Rouby, H., & Collilieux, X. (2017). ITRF2014 plate motion model. *Geophysical Journal International*, *209*(3), 1906–1912.

Bondár, I., & Storchak, D. (2011). Improved location procedures at the international seismological centre. *Geophysical Journal International*, *186*(3), 1220–1244.

Dalaison, M., & Jolivet, R. (2020). A Kalman filter time series analysis method for InSAR. *Journal of Geophysical Research: Solid Earth*, *125*(7), e2019JB019150.

DeMets, C., Gordon, R. G., & Argus, D. F. (2010). Geologically current plate motions. *Geophysical Journal International*, *181*(1), 1–80.

Duputel, Z., Agram, P. S., Simons, M., Minson, S. E., & Beck, J. L. (2014). Accounting for prediction uncertainty when inferring subsurface fault slip. *Geophysical Journal International*, *197*(1), 464–482.

Dziewonski, A., Chou, T.-A., & Woodhouse, J. (1981). Determination of earthquake source parameters from waveform data for studies of global and regional seismicity. *Journal of Geophysical Research: Solid Earth*, *86*(B4), 2825–2852.

Ekström, G., Nettles, M., & Dziewoński, A. (2012). The global CMT project 2004–2010: Centroid-moment tensors for 13,017 earthquakes. *Physics of the Earth and Planetary Interiors*, *200*, 1–9.

Isc on-line bulletin. (2020). International Seismological Centre. doi: 10.31905/D808B830

Kakar, N., Kakar, D. M., Khan, A. S., & Khan, S. D. (2016). Land subsidence caused by groundwater exploitation in Quetta valley, Pakistan. *International Journal of Economic and*

Environmental Geology, *7*(2), 10–19.

Kreemer, C., Blewitt, G., & Klein, E. C. (2014). A geodetic plate motion and global strain rate model. *Geochemistry, Geophysics, Geosystems*, *15*(10), 3849–3889.

Radiguet, M., Cotton, F., Vergnolle, M., Campillo, M., Valette, B., Kostoglodov, V., & Cotte, N. (2011). Spatial and temporal evolution of a long term slow slip event: the 2006 Guerrero slow slip event. *Geophysical Journal International*, *184*(2), 816–828.

Ruleman, C., Crone, A., Machette, M., Haller, K., & Rukstales, K. (2007). *Map and database of probable and possible Quaternary faults in Afghanistan* (Open-File Report No. 1103). U.S. Geological Survey.

Salvatier, J., Wiecki, T. V., & Fonnesbeck, C. (2016). Probabilistic programming in python using PyMC3. *PeerJ Computer Science*, *2*, e55.

Savage, J., & Burford, R. (1973). Geodetic determination of relative plate motion in central California. *Journal of Geophysical Research*, *78*(5), 832–845.

Scordilis, E. (2006). Empirical global relations converting MS and Mb to moment magnitude. *Journal of seismology*, *10*(2), 225–236.

Szeliga, W., Bilham, R., Kakar, D. M., & Lodi, S. H. (2012). Interseismic strain accumulation along the western boundary of the Indian subcontinent. *Journal of Geophysical Research: Solid Earth*, *117*(B08404). doi: 10.1029/2011JB008822